

Deformation statistics of sub-Kolmogorov-scale ellipsoidal neutrally buoyant drops in isotropic turbulence

L. Biferale^{1,†}, C. Meneveau² and R. Verzicco^{3,4}

¹Department of Physics and INFN, Università di Roma ‘Tor Vergata’, Roma, Italy

²Department of Mechanical Engineering, Johns Hopkins University, Baltimore, MD 21218, USA

³Department of Industrial Engineering, Università di Roma ‘Tor Vergata’, Roma, Italy

⁴PoF and MESA+, University of Twente, Enschede, The Netherlands

(Received 14 January 2014; revised 23 May 2014; accepted 21 June 2014;
first published online 30 July 2014)

Small droplets in turbulent flows can undergo highly variable deformations and orientational dynamics. For neutrally buoyant droplets smaller than the Kolmogorov scale, the dominant effects from the surrounding turbulent flow arise through Lagrangian time histories of the velocity gradient tensor. Here we study the evolution of representative droplets using a model that includes rotation and stretching effects from the surrounding fluid, and restoration effects from surface tension including a constant droplet volume constraint, while assuming that the droplets maintain an ellipsoidal shape. The model is combined with Lagrangian time histories of the velocity gradient tensor extracted from direct numerical simulations (DNS) of turbulence to obtain simulated droplet evolutions. These are used to characterize the size, shape and orientation statistics of small droplets in turbulence. A critical capillary number is identified associated with unbounded growth of one or two of the droplet’s semi-axes. Exploiting analogies with dynamics of polymers in turbulence, the critical capillary number can be predicted based on the large deviation theory for the largest finite-time Lyapunov exponent quantifying the chaotic separation of particle trajectories. Also, for subcritical capillary numbers near the critical value, the theory enables predictions of the slope of the power-law tails of droplet size distributions in turbulence. For cases when the viscosities of droplet and outer fluid differ in a way that enables vorticity to decorrelate the shape from the straining directions, the large deviation formalism based on the stretching properties of the velocity gradient tensor loses validity and its predictions fail. Even considering the limitations of the assumed ellipsoidal droplet shape, the results highlight the complex coupling between droplet deformation, orientation and the local fluid velocity gradient tensor to be expected when small viscous drops interact with turbulent flows. The results also underscore the usefulness of large deviation theory to model these highly complex couplings and fluctuations in turbulence that result from time integrated effects of fluid deformations.

Key words: breakup/coalescence, drops and bubbles, homogeneous turbulence

† Email address for correspondence: biferale@roma2.infn.it

1. Introduction

Improving understanding and characterization of drop deformations and possible breakup in turbulent flows is relevant to a wide range of applications, including engineering processes such as emulsification, homogenization, mixing, blending and multiphase chemical reactions (Davies 1985; Lefebvre 1989; Sundaresan 2000). Transport and mixing processes occurring during oil spills and design of remediation strategies also depend critically upon knowledge of oil droplet dynamics and breakup processes occurring in the ocean (Li & Garrett 1998; Yang, Chamecki & Meneveau 2014).

Models for the breakup process are dependent upon characterization of the droplet deformations that precede and facilitate breakup. Much work has focused on breakup and deformations in turbulence when drops are larger than the Kolmogorov dissipation length. The phenomenological model proposed by Kolmogorov (1949) and Hinze (1955) focuses on distorting turbulent stresses as a function of scale in the inertial range and compares these with the restoring forces owing to surface tension. This phenomenological model forms the basis of most of the current models for predicting drop breakup in turbulent flows. Numerical simulations based on fully resolved fluid–fluid interface have also been recently performed to study such complex situation (Perlekar *et al.* 2012). The paper by Lasheras *et al.* (2002) reviews the salient aspects of large droplets subjected to inertial forces. Even without breakup, the understanding of droplet deformation is important in various applications such as predicting effective rheological properties of suspensions or understanding the behaviour of red blood cells interacting with flows including localized large shearing regions. In the latter context several studies have been carried out, relying on an analogy between red blood cells and drops, in order to quantify the haemolysis phenomenon (Arora, Behr & Pasqualis 2006; de Tullio *et al.* 2012).

Deformation of droplets may also be due to purely viscous shear forces rather than inertial ones. This is of particular importance for droplet-laden turbulent flows when droplets are smaller than the Kolmogorov scale. At such scales deformations arise due to viscous drag associated with the shear in the surrounding flow being resisted by surface tension effects. First analyses of droplets in simple viscous shear flow were performed in Taylor (1932). For particular laminar shearing flow, droplets achieve elongated equilibrium shapes. If the shear is strong enough, a droplet may continue to deform and the resistance to deformation due to surface tension is insufficient, leading to unbounded growth of one or two of the droplet's semi-axes. This then provides a possible condition for breakup of droplets when subjected to a simple laminar shear flow. The dimensionless number comparing viscous and surface tension forces is the capillary number $Ca = \mu_o RG/\Lambda$ (μ_o is the surrounding fluid viscosity, R a droplet characteristic scale, G is the shear rate, an inverse timescale, and Λ the surface tension parameter). The capillary number can be used to characterize the critical conditions (a critical capillary number, Ca_c), under which stable stationary droplets are no longer possible and hydrodynamic instabilities develop followed by eventual droplet breakup.

In laminar flow, the external fluid shear can be characterized by one or a few parameters associated with the velocity gradient tensor. Conversely, in a turbulent flow, droplets are subjected to a wide distribution of shear/strain rates. In particular, due to inner intermittency, as the Reynolds number grows so does the range of values of the local strain and/or shearing rates. Locally, these can achieve values that exceed the mean value by a several orders of magnitude. Therefore, one expects that locally some fraction of the droplets will encounter shear rates such that instability and unbounded elongation results. Clearly one would wish to characterize the resulting

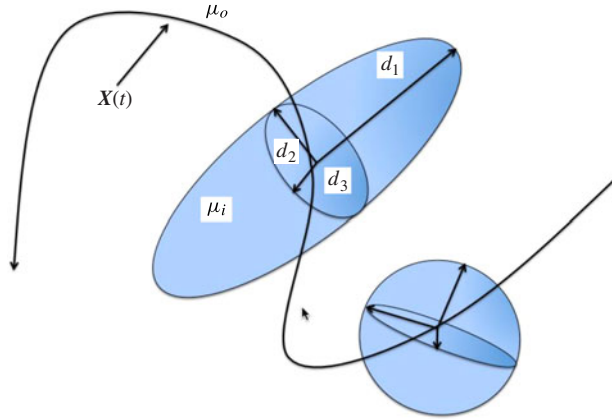


FIGURE 1. (Colour online) Typical ellipsoidal shape of one droplet along the turbulent trajectory. The droplet centre of mass $X(t)$ is supposed to follow the evolution of a fluid particle and the droplet deformation is governed by the statistics of the fluid velocity gradients along the trajectory, $\partial_i u_j(X(t), t)$. We denote by μ_o the viscosity of the carrying fluid and by μ_i that inside the droplet. The droplet is always assumed of ellipsoidal shape with the three semi-axes ordered as $d_1 \geq d_2 \geq d_3$.

droplet dynamics statistically. For example, one is interested in probability distribution functions (p.d.f.) of the characteristic scales (e.g. semi-axes in the case of ellipsoidal droplets), or orientation dynamics of the droplets with respect of the turbulent flows. If some fraction of the droplets is subjected to unbounded elongation, can statistical descriptions still be formulated? How to characterize statistical distributions of small deforming droplets in turbulence remains an interesting challenge that has not received sufficient attention.

Cristini *et al.* (2003) considered the case of droplets that are smaller than the Kolmogorov scale. Detailed calculations that combined simulations of turbulent flows at moderate Reynolds numbers with $Re_\lambda \sim 50\text{--}60$ (λ being the turbulence Taylor microscale) were coupled to a refined boundary integral simulation of local drop dynamics. Such modelling of the droplets was capable of reproducing highly complex shapes such as necks, their instabilities and precursors of satellite droplet formation. Further work along these directions include those from Terashima & Tryggvason (2009) and Can & Prosperetti (2012). However, the turbulent Reynolds numbers that can be considered for such highly detailed simulations are relatively limited. It becomes of interest to seek appropriate simplifications that enable one to explore a broad range of turbulent fluctuations of the shear rates to which small droplets can be expected to be subjected in a turbulent flow at more elevated Reynolds numbers. Assuming that the initial shape of the droplets is spherical, the initial deformations lead to ellipsoidal shapes. Being characterized by three major axes and their orientations, an ellipsoidal drop shape is much easier to describe and parameterize. The fate of deforming ellipsoids in turbulence raises a number of interesting questions such as: denoting the ‘size’ of droplets as the scale of its largest semi-axis d_1 (see figure 1), we may ask what is the resulting p.d.f. of d_1 in turbulence as function of capillary and Reynolds numbers? Under what conditions can equilibrium distribution functions be found? What are the characteristic aspect ratios among largest and smallest semi-axes? Do ellipsoidal droplets tend to be axisymmetric

or triaxial? What are the orientation statistics of deforming droplets? Do their major axes tend to align with the vorticity (as happens with rigid elongated particles) (Parsa *et al.* 2012; Chevillard & Meneveau 2013), do they align with the most extensive strain-rate direction, or with some other direction? How do such orientation trends depend on capillary and Reynolds numbers? How are these alignments related to the deformation rates? These are some of the questions we will address in this paper.

Many models are available for the droplet evolution in turbulent flows. As a first step, it is important to clarify if one is interested in small or large droplets (with respect to the Kolmogorov scale), if they are passive tracers or have a feedback on the flow, if the collision/aggregation of different droplets can be neglected (large dilution limit), if they have inertia (i.e. their centre of mass follows or diverges from a fluid particle trajectory). Finally one also needs to specify the flow properties of the carrier fluid. In this study we apply several simplifying assumptions in order to be able to exploit state-of-the-art numerical simulations of turbulent flows and to track many droplets simultaneously. We focus on the simple (but still interesting) case of sub-Kolmogorov-scale inertialess droplets, in the highly diluted case, therefore neglecting the feedback on the flow and the interactions between different droplets. Moreover, we assume that the droplet shape can be parameterized by an ellipsoid. Even considering this basic case, different models can be adopted. Among them, a popular one has been proposed by Maffettone & Minale (1998) (hereafter referred to as the ‘M&M model’). This model is based on the idea that the droplet deformation is the result of the balance between the local stretching terms of the velocity gradient and the restoring surface tension force. An extra nonlinear constraint is added in order to enforce the preservation of the droplet volume during its evolution. The above dynamics can be parameterized by introducing two functions which depend only on the viscosity ratio between the droplet and the surrounding fluid.

In the present work we examine the fate of small ellipsoidal droplets being transported and distorted by homogeneous isotropic turbulence following the M&M model. We study different statistical properties of the droplets’ shape and its correlation with the underlying turbulent fluctuations when changing the viscosity ratio. It is worthwhile noticing that, when the surrounding fluid and the droplet inner fluid have the same viscosity, the M&M model is very similar to studying the advection/stretching of a small fluid volume together with a relaxation towards a spherical shape. This is also the set-up describing the evolution of the second-order conformation tensor of simple passive polymers in the Oldroyd-B model. In both cases, the deformation rate can be predicted in terms of the statistics of the Lyapunov exponents governing the chaotic properties of particle trajectories; we will exploit this similarity in order to predict the critical capillary number Ca_c where all droplets will break with probability one for such viscous ratio.

However, when the viscosity ratio of the fluids strongly differs from unity, the above analogy does not hold and the prediction of the critical capillary number fails. While many typical applications have viscosity ratios different from unity (e.g. oil droplets in water), the present analysis for unity viscosity ratio is still of interest since there are examples of real liquids with viscosity ratios equal to or close to one that are relevant in technology or nature. One of them is the pair polydimethylsiloxane/polyisobutylene that are both Newtonian fluids, widely used as lubricants and in a large variety of other applications. Their dynamic viscosities at 23 °C are, respectively, 103 and 101 Pa s and their interfacial tension is 2.4 mN m⁻¹ (Guido, Minale & Maffettone 2000a). Another relevant context is the red blood cells in the plasma matrix: in this case the viscosity ratio between the haemoglobin inside

the cells and the plasma is less well defined since it depends on the link with O_2 or CO_2 of the haemoglobin molecules and on the inner cell cytoskeleton consisting of proteins. Nevertheless a viscosity ratio in the range 3–5 is commonly adopted as a reasonable parameter for a healthy human being (Pozrikidis 2003). In this case the role of the surface tension is played by the cell cytoplasmatic membrane.

The paper structure is as follows: in the next section the M&M model is described and briefly derived so that the actions on the droplet of its different terms can be understood. As stated before, the shape dynamics depends upon the Lagrangian time history of the strain and rotation rates of the surrounding turbulent fluid. Full direct numerical simulations (DNS) of turbulence can provide such information (Benzi *et al.* 2010) under the assumption of one-way coupling. The latter has been used extensively to study particle relative dispersion (Bec *et al.* 2010), Lagrangian statistics properties of turbulence (Meneveau 2011) and the fate of non-isotropic particles in turbulence (Parsa *et al.* 2012; Chevillard & Meneveau 2013). In § 3 we simulate an ensemble of droplets, each drop obeying the M&M model following the Lagrangian trajectories of fluid particles in DNS, at two Reynolds numbers. Statistical characterizations of resulting droplet sizes are provided based on the p.d.f. of the largest diameter (the ellipsoid's largest principal axis). Particular attention is placed on the tails of the distributions, to explore the fate of the most deformed droplets and how often these phenomena occur. Viscous drops deform because of hydrodynamical stresses and tend to maintain their shape owing to surface tension. Polymers, described by purely elastic springs, share similar characteristics and analogies with the case of polymers will thus prove useful. Polymers in turbulent flows in fact may undergo the so-called coil-stretch transition if the local straining exceeds the restoring spring force of the polymer for a time long enough during the particle evolution. Such transition can be described by the tendency toward an unbounded growth of the polymer conformation tensor for continuum models as, e.g. the Oldroyd-B (Balkovsky, Fouxon & Lebedev 2000; Boffetta, Celani & Musacchio 2003).

In § 4 the p.d.f.s of droplet sizes are related to the large deviation theory of the largest finite-time Lyapunov exponent (FTLE) for the case of unity viscosity ratio. The formalism can be used to make quantitative predictions of the critical capillary number above which moments of the droplet size distribution diverge. The results from DNS are compared with these theoretical predictions.

In addition to the droplet size distribution, one is also interested in statistical characterizations of droplet shapes and orientations with respect to the local flow. Such properties are evaluated based on DNS and the M&M model, and are presented in § 5. Variations of the ratio of droplet to carrier fluid viscosities are examined in § 6. Conclusions are presented in § 7.

2. Lagrangian model for viscous, tri-axial ellipsoidal droplets in viscous shear flow

The model proposed by Maffettone & Minale (1998) considers a drop of a viscous Newtonian fluid immersed in another viscous Newtonian liquid of the same density, subjected to flow such that an ellipsoidal drop shape of constant volume is maintained at all times. Of course, at significant deformations and especially close to the break-up the ellipsoidal shape is lost. However, some results (Guido & Villone 1998) support the idea that deformations away from ellipsoidal shapes develop only close to the critical shape. Under the assumption of ellipsoidal shape, the drop morphology and orientation can be entirely described by a positive-definite second-order tensor M_{ij} .

The tensor \mathbf{M} is symmetric and its three eigenvalues correspond to the square of the semi-axes length while the eigenvectors give the orientations of the ellipsoid's axes. It can be understood as the inertia tensor of a droplet with constant density ρ_d :

$$M_{ij}(\mathbf{X}(t), t) = \rho_d \int_V (r_i - X_i(t))(r_j - X_j(t)) dV, \quad (2.1)$$

where the integral is extended over the whole volume of the droplet around the instantaneous position of its centre of mass, $\mathbf{X}(t)$.

In the M&M model the drop deformation and orientation dynamics is modelled using the rotation and strain rate of the underlying flow field (whose velocity components are u_i), $\Omega_{kj} = 0.5(\partial_j u_k - \partial_k u_j)$ and $S_{kj} = 0.5(\partial_j u_k + \partial_k u_j)$ as

$$\frac{dM_{ij}}{dt} = \Omega_{ik}M_{kj} - M_{ik}\Omega_{kj} + f_2(\mu)(S_{ik}M_{kj} + M_{ik}S_{kj}) - \frac{f_1(\mu)}{\tau}(M_{ij} - g(\text{II}_M, \text{III}_M)\delta_{ij}), \quad (2.2)$$

where f_1 and f_2 are two functions that depend upon $\mu = \mu_i/\mu_o$ (the ratio of viscosities of the inner, μ_i , and outer, μ_o , fluids), $\tau = \mu_o R/\Lambda$ is the drop/bubble shape relaxation timescale and R the initial radius of the droplet (which is assumed spherical, initially). In (2.2) the first two terms on the right-hand side stem from the local rotation rate while the terms multiplied by f_2 define the stretching due to viscous forces. The last term, proportional to f_1 , models the tendency to restore the spherical shape induced by surface tension effects. Also,

$$g(\text{II}_M, \text{III}_M) = 3 \frac{\text{III}_M}{\text{II}_M} \quad (2.3)$$

enforces exact conservation of the droplet volume at all times as demonstrated by Maffettone & Minale (1998). The factor $g(\text{II}_M, \text{III}_M)$ depends upon the invariants of \mathbf{M} :

$$\text{I}_M = M_{kk}, \quad \text{II}_M = -\frac{1}{2}(M_{ij}M_{ij} - \text{I}_M^2), \quad \text{III}_M = \frac{1}{3}(M_{ik}M_{kj}M_{ji} - \text{I}_M^3 + 3\text{I}_M\text{II}_M). \quad (2.4a-c)$$

Possible expressions for the rotation and stretching prefactors f_1, f_2 which match the known exact asymptotic limits for small Ca , for infinite viscous ratio $1/\mu \rightarrow 0$ and for $\mu = 1$ are given by Maffettone & Minale (1998) as

$$f_1(\mu) = \frac{40(\mu + 1)}{(2\mu + 3)(19\mu + 16)}; \quad f_2(\mu) = \frac{5}{2\mu + 3}. \quad (2.5a,b)$$

A number of other droplet models exist and Minale (2010) provides a review of the many other approaches available to predict droplet dynamics and deformations in viscous flows. Here we use the above M&M model because of its relative simplicity and successful testing under various smooth flow conditions (Guido, Minale & Maffettone 2000b; Minale 2004, 2008, 2010). For neutrally buoyant small droplets placed in a turbulent flow, the Lagrangian evolution of (2.2) must be solved together with the droplet position advected as a fluid particle.

For future reference and convenience, we also provide a dimensionless version of the M&M model that uses the velocity gradients (i.e. the small-scale turbulence inverse timescale) to normalize time, and the initial droplet size to normalize

length-scales (although since the dynamics is homogeneous with \mathbf{M} , its non-dimensionalization is not relevant). The reference inverse turbulent timescale we use is defined as

$$G_t = \left\langle \left(\frac{\partial u_1}{\partial x_1} \right)^2 \right\rangle^{1/2}. \quad (2.6)$$

Also, we define a capillary number according to

$$Ca = \frac{\mu_o R G_t}{\Lambda} = \tau G_t. \quad (2.7)$$

Defining $S'_{ij} = S_{ij}/G_t$, $\Omega'_{ij} = \Omega_{ij}/G_t$, and $t' = tG_t$, the equations are written in dimensionless form as follows:

$$\frac{dM_{ij}}{dt'} = [f_2(S'_{ik}M_{kj} + M_{ik}S'_{kj}) + \Omega'_{ik}M_{kj} - M_{ik}\Omega'_{kj}] - \frac{f_1}{Ca} \left(M_{ij} - 3 \frac{\text{III}_M}{\text{II}_M} \delta_{ij} \right). \quad (2.8)$$

Another characteristic timescale exists, the Lagrangian correlation time of the velocity gradient tensor elements. This correlation determines the temporal persistence of the applied straining and rotation rates. It is known that the correlation timescales of the strain rate and vorticity differ (Guala *et al.* 2007; Yeung *et al.* 2007; Yu & Meneveau 2010*a,b*) but both are known to scale with the Kolmogorov timescale. Hence, they are of the order of $1/G_t$, but possibly with a large prefactor in the case of vorticity.

Among others, we are interested in determining whether there is a steady-state solution for the ‘size’ of the droplets defined in terms of the three semi-axes of its ellipsoidal shape. Let us denote the eigenvalues of \mathbf{M} as d_1^2 , d_2^2 and d_3^2 , ordered according to $d_1 > d_2 > d_3$ and where d_1 , d_2 and d_3 are the ellipsoid’s semi-axes. We recall that the volume constraint implies that $d_1 d_2 d_3$ (strictly speaking the determinant $\det(\mathbf{M}) = d_1^2 d_2^2 d_3^2$) remains constant in time. For large deformations, i.e. $d_1 \gg d_3$, the trace of \mathbf{M} ($I_M = d_1^2 + d_2^2 + d_3^2$) provides information essentially on the largest semi-axis.

3. Results from DNS

In this section, numerical solutions of (2.2) are presented. As mentioned in the previous section, we consider the case of droplets with a size much smaller than the viscous scale and with a negligible mismatch in density with the surrounding fluid. Under these conditions, the droplet centre of mass evolves as a passive tracer in the fluid and we can extract the time history of the velocity gradients along the Lagrangian trajectories of point-like particles following the equation:

$$\dot{\mathbf{X}} = \mathbf{u}(\mathbf{X}(t), t), \quad (3.1)$$

where the Eulerian flow evolves according to the three-dimensional Navier–Stokes equations:

$$\partial_t \mathbf{u} + \mathbf{u} \cdot \nabla \mathbf{u} = -\nabla p + \nu \nabla^2 \mathbf{u} + \mathbf{F}, \quad \nabla \cdot \mathbf{u} = 0. \quad (3.2)$$

The Lagrangian signals for the velocity gradient time histories, $\partial_i u_j(\mathbf{X}(t), t)$, are obtained from DNS of homogeneous isotropic turbulence at two Reynolds numbers. The details about the DNS are given in table 1 (more details about the statistical properties of the Eulerian and Lagrangian fields can be found in Cencini *et al.* (2006) and Bec *et al.* (2010)): The statistically homogeneous and isotropic external

	N	Re_λ	η	δx	ε	ν	τ_η	t_{dump}	δt	T_L	G_I
Run I	512	185	0.01	0.012	0.9	0.002	0.047	0.004	0.0004	2.2	5.48
Run II	2048	400	0.0026	0.003	0.88	0.00035	0.02	0.00115	0.000115	2.2	11.4

TABLE 1. Eulerian parameters for the two sets of data from the DNS of homogeneous and isotropic turbulence. Here N is the number of grid points in each spatial direction; Re_λ is the Taylor-scale Reynolds number; η is the Kolmogorov dissipative scale; $\delta x = \mathcal{L}/N$ is the grid spacing, with $\mathcal{L} = 2\pi$ denoting the physical size of the numerical domain; $\tau_\eta = (\nu/\varepsilon)^{1/2}$ is the Kolmogorov dissipative timescale; ε is the average rate of energy injection; $\nu = \mu_0/\rho$ is the kinematic viscosity; t_{dump} is the time interval between two successive data recordings along particle trajectories; δt is the time step of the model integration; $T_L = L/U_0$ is the eddy turnover time at the integral scale $L = \pi$, U_0 is the typical large-scale root-mean-square velocity and G_I is the reference inverse turbulent timescale. Averages are performed over two large eddy turnover times.

forcing \mathbf{F} injects energy in the first low-wavenumber shells, by keeping constant their spectral content (Chen *et al.* 1993). The kinematic viscosity $\nu = \mu_0/\rho$ is chosen such that the Kolmogorov length scale $\eta \approx \delta x$, where δx is the grid spacing; this choice ensures a good resolution of the small-scale velocity dynamics. The numerical domain is cubic and 2π -periodic in the three directions of space. We use a fully dealiased pseudospectral algorithm with second-order Adam–Bashforth time-stepping (for details see Bec *et al.* (2006) and Cencini *et al.* (2006)). We analyse data from two series of DNS: run I with numerical resolution of 512^3 grid points, and the Reynolds number at the Taylor microscale $Re_\lambda \approx 185$; Run II with 2048^3 resolution and $Re_\lambda \approx 400$. Particle trajectories are recorded at a frequency of $t_{dump} \sim \tau_\eta/10$ and followed for a total time of the order of $2T_L$, with T_L the large eddy turnover time of the turbulent flow. We analyse a total of 15×10^3 and 7×10^3 trajectories for Run II and Run I, respectively. The integration of (2.2) is further refined by making a linear time interpolation by a factor 10 between two successive recorded data points along the Lagrangian trajectory.

The evolution of the morphology tensor is stopped when the maximum deformation, defined as the ratio between d_1/d_3 exceeds a factor 10^3 . While this is an arbitrary criterion to define a threshold associated with possible subsequent droplet breakup, it has been verified by various numerical tests (see below) that the dominant features of droplet dynamics and statistics show little sensitivity to the threshold value. More advanced criteria taking into account droplet shape instabilities could be used, but especially under the limiting assumption that the shape remains ellipsoidal, this simple type of criterion is deemed appropriate for the focused objectives of this study.

The initial drop size is assumed to be sufficiently smaller to the Kolmogorov scale η so that even after severe deformations the largest scale still falls within the viscous range. The cut-off ratio $d_1/d_3 = 10^3$ means, due to the volume conservation, that d_1 is at most a factor of 100 times the original scale. In practice the viscous range extends to scales of the order of 10η so that effectively, we are assuming that the initial scale is smaller or equal to $\eta/10$. Note that due to the homogeneity of (2.2), we can rescale M_{ij} using the initial radius as characteristic length scale without modifying the equation. Therefore, the initial physical length scale of the droplet does not explicitly enter into the dynamics, except through the relaxation timescale τ .

We begin by showing some typical time evolutions of droplets for different values of the capillary number. In figure 2 we show the time evolution of the square root

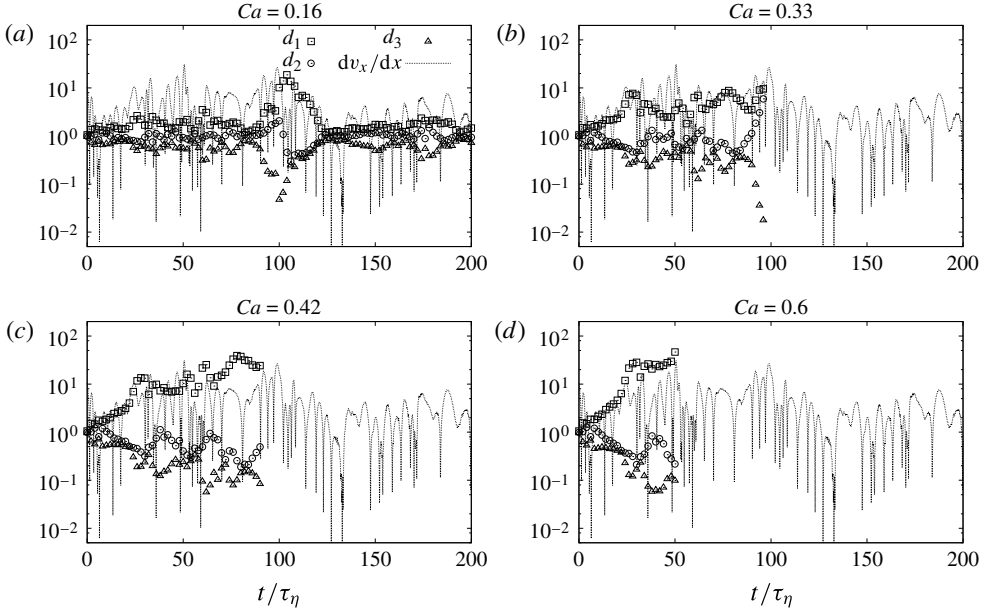


FIGURE 2. Time signals of the square root of the eigenvalues, $d_1(t)(= [\lambda_m^{(1)}]^{1/2})$, $d_2(t)$ and $d_3(t)$ in logarithmic units obtained from solving the M&M droplet model coupled to Lagrangian time history of turbulent velocity gradients from DNS at $Re_\lambda = 185$. We also superpose the time history of $|A_{11}(t)|$, the absolute value of one component of the velocity gradient tensor (solid line).

$d_i(t) = (\lambda_m^{(i)})^{1/2}$ of the three morphology tensor eigenvalues for different relaxation times τ , and for $\mu = 1$, along a sample droplet trajectory. As one can see, at increasing relaxation time, i.e. increasing capillary number for a given turbulence intensity, the droplet tends to deform more and more. For instance, the time history here represented shows a peak in the deformation at a time $t \sim 100\tau_\eta$ during the droplet evolution where only the droplet with $Ca = 0.16$ survives since it did not exceed the $d_1/d_3 = 10^3$ threshold.

In figure 3 we show an enlargement of this event, where one can better see the transition from an oblate to a strongly prolate shape during the droplet evolution. Only later does the surviving droplet recover a spherical-like shape with $d_1 \sim d_2 \sim d_3 \sim 1$. In figure 3(b) we show the time history of the three diagonal components of the velocity gradient tensor, in order to highlight the noticeable correlation between events where the droplet is strongly deformed and the underlying turbulent fluctuations of the fluid velocity field rate of deformation. As one can see, the event around $t \sim 100\tau_\eta$, where droplets with large capillary number break, is preceded by strong intense oscillations in the turbulent stretching rates.

As a next step, we focus on the distribution of droplet sizes. Figure 4 shows the p.d.f.s of the largest \mathbf{M} eigenvalue, $\lambda_m^{(1)} = d_1^2$, for various values of Ca for both runs at the two Reynolds numbers. As can be seen for increasing capillary number, when the surface tension is decreased (for a fixed mean turbulent straining timescale), longer tails develop and very large droplet deformation can occur. The tails approach a power-law form $P(x) \sim x^{-q}$ with q decreasing (i.e. the tails becoming less steep) at increasing capillary number. Similar behaviour can be observed at larger Reynolds numbers as shown in the (b) of the same figure.

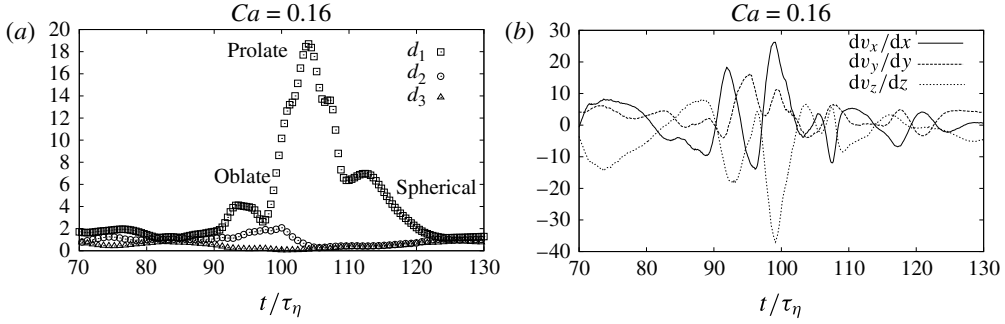


FIGURE 3. (a) Enlargement of the previous figure for $Ca = 0.16$ around the peak of the deformation of the droplet. (b) The corresponding evolution for the three diagonal entries of the velocity gradient tensor, $A_{11}(t)$, $A_{22}(t)$, $A_{33}(t)$.

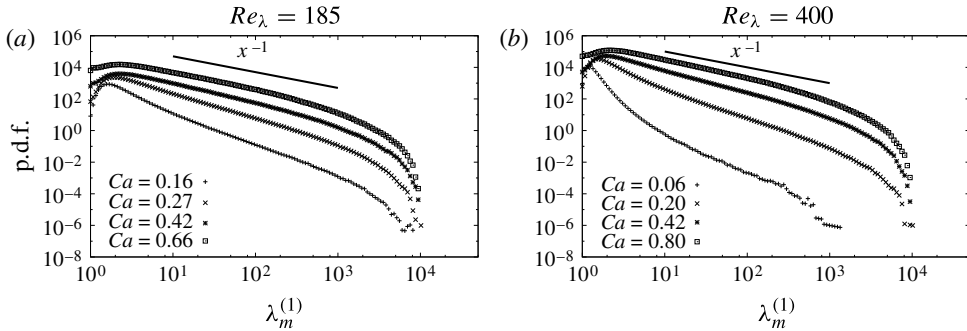


FIGURE 4. Probability density functions of largest eigenvalue $\lambda_m^{(1)}$ of the morphology tensor \mathbf{M} , obtained from solving the M&M droplet model coupled to Lagrangian time history of turbulent velocity gradients from DNS at (a) $Re_\lambda = 185$ and (b) $Re_\lambda = 400$. Different curves correspond to different values of the capillary number, both below and above the critical value, $Ca_c \sim 0.42$. The solid line represents the power-law behaviour $\propto x^{-1}$. Curves are shifted vertically for the sake of presentation.

At capillary numbers above a threshold value, it is apparent that the p.d.f. develops a -1 power-law tail, $q \rightarrow 1$.

For such tails, while for finite size systems we may operationally measure the p.d.f.s due to the finite threshold imposed (we cannot exceed a maximum ratio between the highest and the lowest eigenvalue), if one were to imagine a system without such cutoffs, the p.d.f. could not be normalized because its integral diverges at large values. The transition to this behaviour appears to occur near $Ca_c \approx 0.4$ for both $Re_\lambda = 185$ and $Re_\lambda = 400$. We interpret such transition as follows: for $Ca > Ca_c$ if one waits long enough, with probability equal to unity all droplets would break eventually. For smaller Ca , breaking is still possible for some droplets (as, e.g., shown in figure 2), but large deformations become exponentially less probable. In the next section an attempt will be made to predict this critical value of Ca based on knowledge about turbulence small-scale statistics.

In figure 5 we show the dependence of the p.d.f.s on the d_1/d_3 threshold chosen as a criterion for droplet breakup, i.e. as a rule to stop the droplet trajectory. As is quite apparent, increasing the threshold leads to longer and longer tails of the p.d.f.

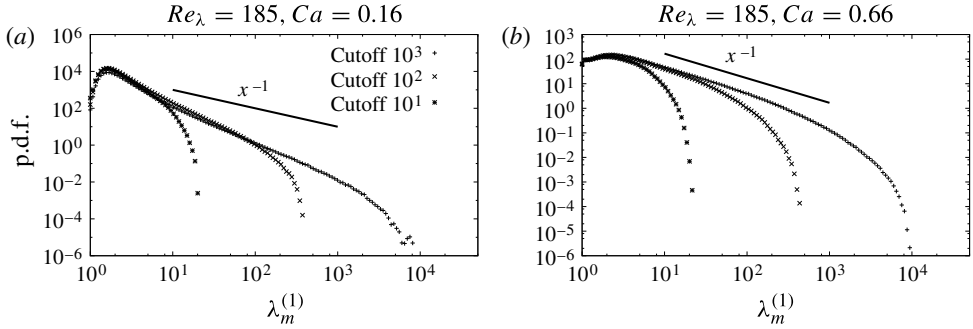


FIGURE 5. Probability density functions of largest eigenvalue $\lambda_m^{(1)}$ of the morphology tensor \mathbf{M} , obtained from solving the M&M droplet model coupled to Lagrangian time history of turbulent velocity gradients from DNS at $Re_\lambda = 185$. Different symbols denote different imposed cutoff values for the maximum deformation value $d_1/d_3 = 10, 10^2, 10^3$. Results are shown for two capillary numbers $Ca = 0.16$ below (a) and above (b) Ca_c . We also superpose the power-law behaviour $\propto x^{-1}$ predicted for the saturation slope when $Ca > Ca_c$.

without changing its main features. Using high threshold values enables us to exhibit the power-law scaling of the p.d.f. that develops for large-scale disparities d_1/d_3 .

4. Cramer function formalism and FTLEs

In this section we aim at establishing a semi-analytical tool to predict the p.d.f. shape of the maximal elongation of the droplet in the case when the viscosity ratio is unity, $\mu = 1$. In such a case, the stretching and the rotation terms of the M&M model coincide with those describing the stretching and rotation of an infinitesimal volume of the fluid and therefore can be connected to the statistics of the Lyapunov exponent of the particle trajectories inside the turbulent flow (Bec *et al.* 2006). It is useful in this case to return to the dimensional description, (2.2), in order to have a clearer understanding of the physical origin of all terms. When $f_2 = 1$ (viscosity ratio unity) the rotation rate and deformation rate tensors sum up to give the following evolution for the morphology tensor of the droplet:

$$\frac{dM_{ij}}{dt} = (A_{ik}M_{kj} + M_{ik}A_{kj}) - \frac{f_1}{\tau} (M_{ij} - g(\text{III}_M, \text{II}_M)\delta_{ij}), \quad (4.1)$$

where everything is expressed in terms of the velocity gradients, $A_{ik} = \partial u_i / \partial x_k$. It is useful here to point out that the evolution given by (4.1) is very close to that of polymer stretching by a turbulent flow as for the case of the approximation given by the Oldroyd-B model. In the latter the role played by the morphology tensor \mathbf{M} is played by the polymer conformation tensor $C_{ij}(\mathbf{X}(t), t) = \bar{R}_i \bar{R}_j$ (where \mathbf{R} is the ‘ends-to-ends polymer vector’ and the average is intended over the thermal noise applied to each molecule inside an infinitesimal volume advected by the flow, see Balkovsky *et al.* (2000) and Chertkov (2000) for a rigorous discussion). For the polymer case, the linear damping is given by a relaxation timescale toward the equilibrium isotropic extension. The only difference between the two cases is that for polymer there is no need to enforce the volume conservation and therefore the term g is typically set to unity in an equation such as (4.1). For the tails of the probability distribution of the

largest eigenvalue of \mathbf{M} , these differences are expected to have negligible effects since along the tail we have $\text{Tr}(\mathbf{M}) \gg 1$ and in that limit $M_{ij} - g\delta_{ij} \approx M_{ij}$ (g tends to zero since II_M grows while III_M remains unity). The long time evolution of the droplet morphology tensor, given by (4.1), will depend critically upon the balance between two different mechanisms: the first is given by the accumulation of the stretching effects induced by the underlying flow, as expressed by the terms $(A_{ik}M_{kj} + M_{ik}A_{kj})$ on the right-hand side of (4.1). The second mechanism is given by the relaxation toward an isotropic configuration as expressed by the term $(f_1/\tau)(M_{ij} - g\delta_{ij})$. If the former is strong enough to dominate the long-term behaviour, the droplet will be in a stretched configuration (and it keeps stretching with one or two of its length scales growing in an unbounded fashion if not resisted by additional nonlinear stiffness mechanisms). In the opposite case it will be, on average, in a coiled configuration, where we have used this term to stress the analogy with the polymer dynamics. In order to predict the critical capillary number where stretching will overwhelm the surface tension effects it is possible to apply the same balance already successfully used for the polymer case by Balkovsky *et al.* (2000) and Boffetta *et al.* (2003). The idea is to control the asymptotic behaviour of the trace of the morphology tensor, $\text{Tr}(\mathbf{M}(t))$ observing that thanks to (2.1) it is equivalent to the tensorial product of two infinitesimal vectors defining the position of a generic particle inside the droplet, $R_i = x_i - X_i(t)$. We therefore can restrict ourself to study the evolution of a fluid line element in the fluid:

$$\frac{dR_i}{dt} = A_{ik}R_k \quad (4.2)$$

and then taking the square of it in a suitable sense. To characterize the long-time evolution of (4.2) it is useful to introduce the so-called FTLEs:

$$\gamma(t) = \frac{1}{t} \log \left(\frac{|\mathbf{R}(t)|}{|\mathbf{R}(0)|} \right), \quad (4.3)$$

which for large t tends with probability one to the largest Lyapunov exponent governing the chaotic properties of particles trajectories in the turbulent flow, $\lambda_L = \lim_{t \rightarrow \infty} \gamma(t)$. However, if we do not perform the limit $t \rightarrow \infty$, the FTLE exhibits deviations from the mean. These fluctuations are described by the p.d.f. of γ at various times via the large deviation theorem (Frisch 1995):

$$P(\gamma, t) \sim \exp(-tS(\gamma)), \quad t \rightarrow \infty. \quad (4.4)$$

The function $S(\gamma)$ is the so-called Cramer function (see Frisch 1995 for a text book introduction and also Eckmann & Procaccia 1986 and Paladin & Vulpiani 1987) which must be convex, semi-positive definite and vanishing at $\gamma = \lambda_L$, because for $t \rightarrow \infty$ we must have with probability one that the FTLE converge to the largest Lyapunov exponent, λ_L . Combining (4.3) and (4.4) one may write for the q th-order moments of the vector growth:

$$\left\langle \left(\frac{|\mathbf{R}(t)|}{|\mathbf{R}(0)|} \right)^q \right\rangle = \int \exp[t(q\gamma - S(\gamma))] d\gamma \sim \exp(tL(q)), \quad (4.5)$$

where the last passage is obtained in the saddle point limit of large t subject to the condition:

$$L(q) = \max(q\gamma - S(\gamma)). \quad (4.6)$$

Moreover, one can show that the Lyapunov exponent $\lambda_L = L'(0) = (dL(q)/dq)|_{q=0}$. We must now just note that the stretching part of the evolution (4.1) is twice the right-hand side of (4.2), i.e. $M_{ij} \sim R_i R_j$. As a result, we have that the large deviation properties of the largest eigenvalue of the morphology tensor are controlled by $L(2q)$ instead of $L(q)$. Considering also the linear relaxation induced by the surface tension terms and neglecting the $O(1)$ terms in fronts to the δ_{ij} , which must not be important when $\text{Tr}(\mathbf{M}) \gg 1$, we end up with the prediction that for large times:

$$\langle [\text{Tr}(\mathbf{M}(t))]^q \rangle \sim \exp \left[t \left(L(2q) - q \frac{f_1}{\tau} \right) \right]. \quad (4.7)$$

It is possible now to derive a criterion for the existence of a stationary probability distribution for the morphology tensor. A stationary p.d.f. must be normalizable at all times, i.e. the exponent $L(2q) - qf_1/\tau$ must be zero when $q = 0$, such that $\lim_{q \rightarrow 0} \int x^q P(x) dx = \int P(x) dx = 1$. The latter condition implies that there exists a critical relaxation time τ^c such that

$$\lim_{q \rightarrow 0} [L(2q) - qf_1/\tau^c] = 0, \quad \text{or} \quad \tau^c = \lim_{q \rightarrow 0} (f_1/L(2q)) = f_1/(2L'(0)) = f_1/(2\lambda_L). \quad (4.8a,b)$$

For $\tau > \tau^c$ the tensor does not reach a stationary distribution and it is indefinitely stretched. In that limit we will have that all moments diverge (which corresponds to the Weissenberg criterion for the coil-stretched transition in the case of polymers). For $\tau < \tau^c$, when the p.d.f. of the trace, $x = \text{Tr}(\mathbf{M})$, is normalizable, the tail will scale like

$$P(x) \sim x^{-(1+\tilde{q}(\tau))}. \quad (4.9)$$

The critical exponent of the tail is given by the largest order of the moment that does not diverge, i.e. $\tilde{q}(\tau)$ is such that

$$L(2\tilde{q}(\tau)) = \frac{f_1 \tilde{q}(\tau)}{\tau}. \quad (4.10)$$

For many practical purposes, the Cramer function $S(\gamma)$ can be expanded in Taylor series around its minimum up to second order,

$$S(\gamma) = (\gamma - \lambda_L)^2 / (2\sigma), \quad (4.11)$$

where σ is a parameter characterizing the degree of intermittency and variability of the FTLE. The Cramer function of Navier–Stokes turbulence in three dimensions has been measured in prior work, based on Lagrangian tracking and integration of fluid velocity gradients from DNS at 512^3 and $Re_\lambda = 185$ (Bec *et al.* 2006). In figure 6 this measured Cramer function is shown and the measured (fitted) λ_L and σ are given in the caption. Let us first note that the Cramer function cannot be exactly parabolic for all values of γ ; this is due to the fact that the incompressibility constraint forces $\gamma > 0$. Nevertheless, it is possible to find a good parabolic fit for the right branch of the parabola, the only one that will be of interest for us because the condition (4.10) gives values of $\tilde{q}(\tau)$ that correspond to $\gamma(\tilde{q}) > \lambda_L$ (see below).

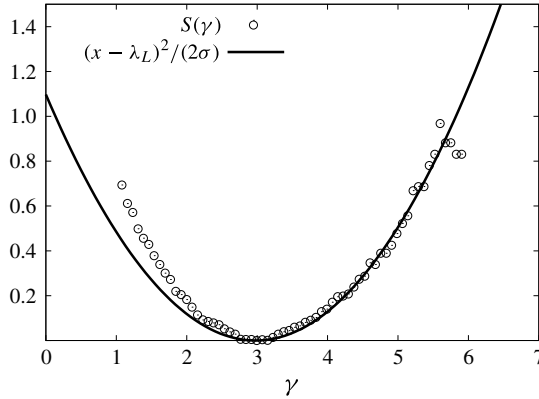


FIGURE 6. Cramer function (from Bec *et al.* 2006). We show also the parabolic fit that uses $\lambda_L = 0.14/\tau_\eta = 2.97$ and $\sigma = 0.19/\tau_\eta = 4.04$ with $\tau_\eta = 0.047$.

4.1. Comparison with DNS

In the DNS used to obtain the results shown in figure 4, the parameters $f_1 = 0.457$ and $f_2 = 1$ (unity viscous ratio) were used. Also, for the DNS flow, the main Lyapunov exponent is $\lambda_L \sim 2.97$ (Bec *et al.* 2006). Therefore, we predict as a critical relaxation timescale the value

$$\tau^c = f_1 / (2\lambda_L) \sim 0.077, \quad (4.12)$$

which in terms of the critical capillary number means $Ca_c = \tau^c \langle (\partial u_1 / \partial x_1)^2 \rangle^{0.5} = 0.42$. This value of critical capillary number or τ^c is very well confirmed by the results shown in figure 4, where the p.d.f.s were shown to saturate to a -1 tail for $\tau \sim 0.077$ ($Ca_c = 0.42$) for the $Re_\lambda = 185$ DNS case. Because the dependency on the Reynolds number enters only via the Lyapunov exponent λ_L , which is known to follow the relation $\lambda_L \sim 0.14/\tau_\eta$ (see Bec *et al.* 2006), it is also possible to predict the critical relaxation time for the $Re_\lambda = 400$ case. In particular, replacing the values for τ_η given in table 2 we must have $\tau^c \sim 0.033$ for $Re_\lambda = 400$, which would correspond to $Ca_c \sim 0.37$ again in good agreement with the observed accumulation of the p.d.f.'s tail shown in figure 4(a). Note that the critical capillary number should at first sight not depend on Reynolds number because the two quantities λ_L and $\langle (\partial u_1 / \partial x_1)^2 \rangle^{0.5}$ have the same Reynolds dependency on dimensional grounds. The numerical results shown in Bec *et al.* (2006) suggest the presence of a small intermittency correction to the rule $\lambda_L \propto 1/\tau_\eta$. Moreover, in order to understand the Reynolds dependency of (2.7) one would need to also consider the intermittent corrections to the statistics of velocity gradients (Benzi *et al.* 1991). It is difficult to say whether the observed small dependency of Ca_c on Reynolds is due to these two combined intermittent corrections or it is just induced by small statistical fluctuations on the measured quantities. Data from a larger variation in Reynolds are needed in order to answer this important question.

Next, we explore whether relation (4.10) can be used to estimate the p.d.f. slopes for $\tau < \tau^c$, i.e. before criticality. Again, we use the published Cramer function (Bec *et al.* 2006) (see figure 6). Using a parabolic fit (4.11), the Legendre transform can be worked out analytically and the maximum is reached for

$$\tilde{\gamma}(q) = \lambda_L + 2\sigma q. \quad (4.13)$$

	$\tau = 0.03$	$\tau = 0.05$	$\tau = 0.06$	$\tau = 0.077$
	$Ca = 0.16$	$Ca = 0.27$	$Ca = 0.33$	$Ca = 0.42$
$\tilde{q}(\tau)$	1.15	0.39	0.21	0

TABLE 2. Values of the asymptotic power-law slopes for the p.d.f. of the trace of the morphology tensor for $Re_\lambda = 185$ simulation, for these parameters we have $\tau^c \sim 0.077$ ($Ca_c \sim 0.42$).

	$\tau = 0.005$	$\tau = 0.015$	$\tau = 0.025$	$\tau = 0.033$
	$Ca = 0.06$	$Ca = 0.2$	$Ca = 0.32$	$Ca = 0.37$
$\tilde{q}(\tau)$	4.1	0.87	0.23	0

TABLE 3. Asymptotic power-law slopes for the p.d.f. of the trace of the morphology tensor for $Re_\lambda = 400$ simulation. For these parameters we have $\tau^c \sim 0.033$, ($Ca_c \sim 0.37$).

Moreover,

$$L(2q) = 2q\lambda_L + 2\sigma q^2, \quad (4.14)$$

which gives the prediction for the slope (from (4.10)):

$$\tilde{q}(\tau) = \frac{f_1/\tau - 2\lambda_L}{2\sigma}. \quad (4.15)$$

The first thing to be noticed is that from (4.13), already for $q = 0.5$ we have $\tilde{\gamma}(1) = \lambda_L + \sigma \sim 7$, i.e. already for $\tilde{q} \sim 0.5$ we are probing the far tails of the Cramer function figure 6. Hence, to remain within good statistical confidence, we can apply the prediction (4.15) only if it is satisfied for $\tilde{q} \ll 1$, i.e. for capillary numbers and relaxation times relatively close to the critical ones. In tables 2 and 3 we report for both Run I and Run II the values for the slopes of the p.d.f. tails using the expressions $\sigma = 0.19/\tau_\eta$ and $\lambda_L = 0.14/\tau_\eta$ which we showed in figure 6 to be a good fit for the right branch of the Cramer function.

In figure 7 we superpose the p.d.f.s of the largest eigenvalue of the morphology tensor \mathbf{M} at different capillary numbers for some typical values given in tables 2 and 3. One can notice that by increasing the capillary number, the theoretical prediction based on the large deviation theory for the FTLE becomes increasingly better. The deviations for $Ca \ll Ca_c$ could be due to the following reasons: first, as said, for small Ca the saddle point estimate is dominated by very large values of the FTLE, leading to a bigger statistical uncertainty; second, if the capillary number is small, the stretching terms are less important, the morphology tensor is closer to its isotropic shape, stretching does not persist for long times and probably the asymptotic estimate of the large deviation Cramer function is not suitable for such intermediate situations.

5. Further characterization of droplet orientations and morphology

In this section, we provide results from the analysis of droplets in DNS not only focusing on the largest eigenvalue as done in the preceding sections, but also characterizing the droplet morphology and orientation dynamics. In order to characterize the shape of the particle, we use the p.d.f. of the deformation parameter also used in Guido *et al.* (2000b):

$$P(D) \quad \text{where } D = \frac{d_1 - d_3}{d_1 + d_3}. \quad (5.1)$$

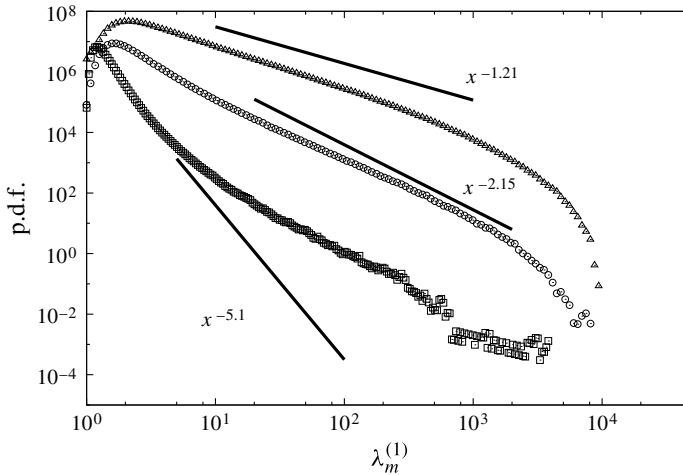


FIGURE 7. P.d.f.s of the largest eigenvalue of the morphology tensor for $Ca = 0.06$ (squares), $Ca = 0.16$ (circles) and $Ca = 0.33$ (triangles) as computed from the simulation. The corresponding theoretical power-law predictions are shown as solid lines with the predicted slopes (exponents) noted.

This parameter does not distinguish between disk-like and cigar-like shapes, but for a sphere one has $D = 0$ and for the most deformed possible states (either disk- or spaghetti-like), one has $D = 1$. In addition, to distinguish also between disk-like and cigar-like shapes, the s^* parameter introduced by Lund & Rogers (1994) to characterize the rate of strain eigenvalues (that add to zero) can be used if properly modified. For this purpose, the eigenvalues must first be redefined in terms of logarithmic variables. We define

$$r_i = \ln(d_i/d_i(0)), \quad (5.2)$$

then $\sum_{i=1}^3 r_i = 0$. We then define the Lund & Rogers (1994) parameter

$$s^* = -3\sqrt{6} \frac{r_1 r_2 r_3}{(r_1^2 + r_2^2 + r_3^2)^{3/2}} \quad (5.3)$$

which is such that $s^* = +1$ indicates disk-like shapes while $s^* = -1$ indicates long fibre-like shapes. However, $s^* = 0$ is somewhat indeterminate: it can mean either a sphere or an ellipsoid in which the intermediate axes remains undeformed with $d_2(t) = d_2(0)$ leading to $r_2 = 0$ and $s^* = 0$. Still, peaks of the p.d.f. of s^* , $P(s^*)$, near either $s^* = \pm 1$ can be interpreted quite clearly.

We present p.d.f.s of the parameters D and s^* in figures 8 and 9, respectively, for various of the Ca considered from the $Re_\lambda = 185$ simulation. From the results for D the trends are clear: for increasing capillary number, the droplets become more and more anisotropic, with an increasing ratio between largest and smallest principal axes. The trends shown in figure 9 for s^* are less monotonic. There is a tendency toward rod-like shape for capillary numbers approaching the critical value, and a small recovery towards more disk-like shapes for very large capillary numbers.

Prior work has studied orientation dynamics and tumbling rates of non-deforming rigid ellipsoidal particles. In particular, e.g. the works of Shin & Koch (2005),

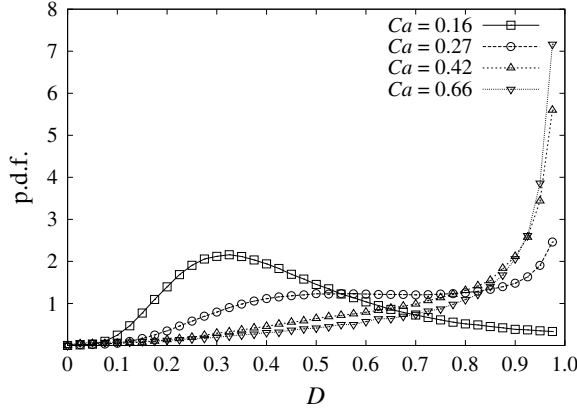


FIGURE 8. P.d.f.s of $D = (d_1 - d_3)/(d_1 + d_3)$, for different Ca .

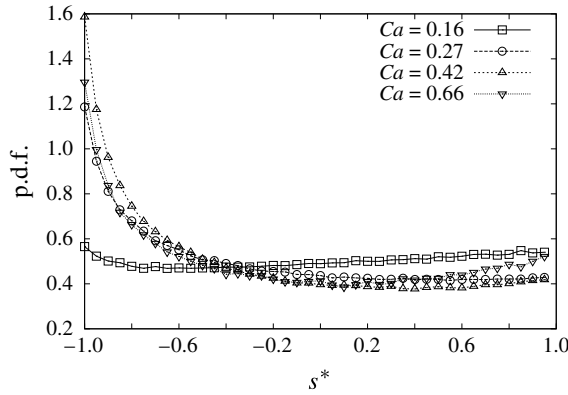


FIGURE 9. P.d.f.s of s^* , for different Ca .

Parsa *et al.* (2012) and Chevillard & Meneveau (2013) show that particles with one elongated direction and two small ones (fibre- or rod-like, $s^* \rightarrow -1$) tend to align with the vorticity, which implies rotation around the major axis thus effectively reducing the tumbling rate of that major axis. As the anisotropy of the particle is increased, its tumbling rate is reduced. Conversely, Parsa *et al.* (2012) have found that the tumbling rates of disk-like particles (two large and one very small major axis, $s^* \rightarrow 1$) is significantly increased. This trend is due to the fact that disk-like particles tend to align with the most contracting eigendirection of the strain-rate tensor which, in turbulence, happens to be preferentially orthogonal to the vorticity vector (Chevillard & Meneveau 2013). The vorticity then spins the disk strongly, not unlike setting a coin spinning on a tabletop. However, if the particle is allowed to deform, these trends can be expected to be modified significantly. Hence, the alignment properties of droplets with the strain rate and vorticity are of considerable interest.

In order to characterize the orientation statistics of droplets relative to the flow field, we are interested in the p.d.f.s of cosine of angles between, $\mathbf{e}_m^{(1)}$, the eigenvector corresponding to the largest semi-axis of the morphology tensor and a few characteristic directions of the underlying flows (we will consider only absolute

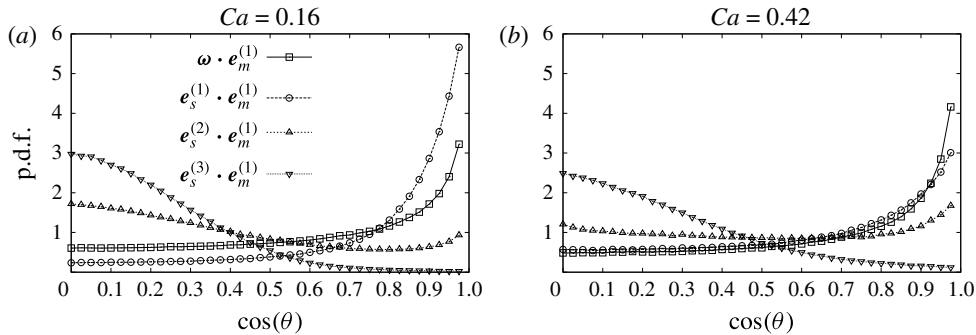


FIGURE 10. P.d.f.s of cosine of angle between the particle's largest eigenvector, $e_m^{(1)}$, with vorticity and the three eigenvectors of \mathbf{S} , for two Ca (a and b).

values of the cosines to avoid problems with direction ambiguities):

$$P(|e_m^{(1)} \cdot \hat{\omega}|), \quad P(|e_m^{(1)} \cdot e_s^{(1)}|), \quad P(|e_m^{(1)} \cdot e_s^{(2)}|), \quad P(|e_m^{(1)} \cdot e_s^{(3)}|), \quad (5.4a-d)$$

where $\hat{\omega}$ is the unit vector in the vorticity direction, and $e_s^{(k)}$ ($k = 1, 2, 3$) are the three orthogonal strain-rate eigendirection unit vectors. In terms of the alignment of the ellipsoids relative to features of the turbulent flow, in figure 10, we show p.d.f.s of the cosine of the angle with each of the four directions characterizing the local turbulent flow: the three strain-rate eigendirections and the vorticity for two different capillary numbers. From these results it is apparent that the droplet largest eigendirection tends to align with the most extensive strain-rate eigendirection, as well as with the vorticity. It also often aligns with the second intermediate strain-rate eigendirection (which itself is well aligned with the vorticity). Conversely, it tends to be orthogonal to the most contracting eigendirection. At increasing capillary number, the alignment is less pronounced, since the droplet has less time to synchronize with the underlying flow topology before it deforms and reaches the threshold deformation levels leading to eventual breakup.

6. Effects of the viscosity ratio

When changing the viscosity ratio $\mu = \mu_i/\mu_o$, we change the relative importance of stretching with respect to rotation in (2.2). In figure 11 we show their functional dependency as a function of μ , as given by the phenomenological dependency of f_2 and f_1 proposed by Maffettone & Minale (1998). We can see that while the ratio f_1/f_2 is always close to 0.45, for large viscosity ratios the values of f_2 and f_1 can change up to a factor 4–5.

Next, it is of interest to attempt to apply our earlier Cramer-function predictions to the case of different viscosity ratios. For instance, for the case at $\mu = 10$, loosely applying an ‘order-of-magnitude’ estimate one would have predicted that the transition to a ‘non-stationary’ regime (unbounded growth of the major axis or axes) would happen when

$$f_2(10)\lambda_L \sim f_1(10)/\tau_c. \quad (6.1)$$

This is because now the stretching part is proportional to f_2 and we are supposing that the symmetric stress tensor, $S_{ij} = (A_{ij} + A_{ji})/2$, leads to the same Lyapunov exponent λ_L as that of the original one, A_{ij} . If this were true, we should expect for the transition

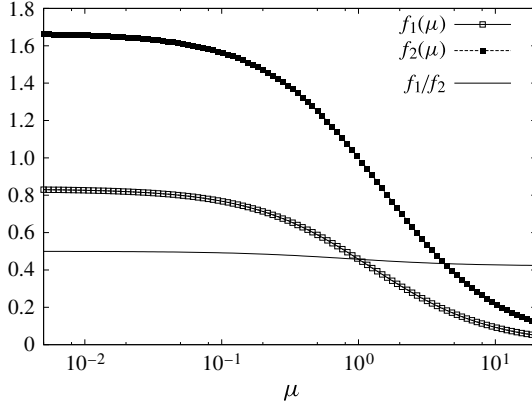


FIGURE 11. Behaviour of $f_1(\mu)$, $f_2(\mu)$ and of their ratio at changing μ . Note that for $\mu \ll 1$ the prefactor in front of the symmetric stress tensor term (the only one which stretches) becomes very small. As a result the deformation of the droplet is much smaller if the capillary number is kept unchanged.

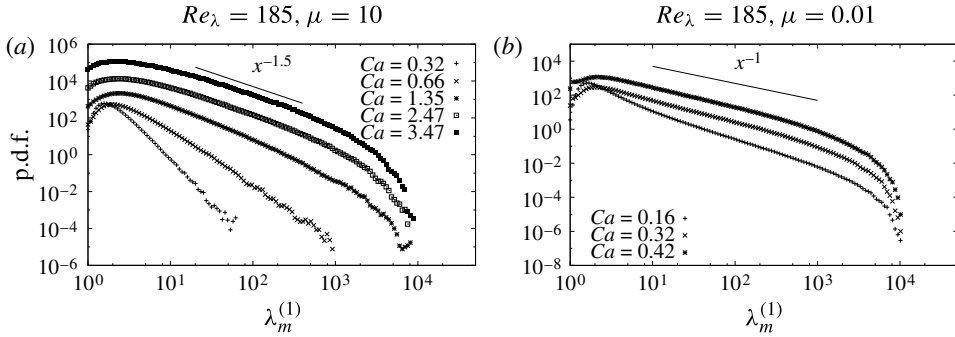


FIGURE 12. (a) P.d.f. of the largest eigenvalue of the morphology tensor for various capillary numbers, for viscosity ratio $\mu = 10$. Note that the straight line has a slope -1.5 and that the saturation of the tails happens at a higher Ca value compared with the critical capillary estimated by (6.1). (b) The same for $\mu = 0.01$. Now the transition is very similar to the case $\mu = 1$, and the tail has the -1 power-law slope.

to occur at $Ca_c \sim 0.81$ (because from (6.1) we have $\tau^c = f_1(10)/f_2(10)\lambda_L^{-1} = 0.148$, and with $G_t = 5.48$ we obtain $Ca_c = \tau^c G_t = 0.81$). This, however, is not what is observed in the numerical results shown in figure 12. As one can see in figure 12(a), the saturation seems to be present, but now at around $Ca_c \sim 2.5$, i.e. it is delayed. This might be understood heuristically by noting that the rotation is decorrelating the droplet orientation from the stretching rate thus making strong deformations less likely. Moreover the slope of the p.d.f. is not close to -1 , meaning that the physics of the deformations and relaxations, and its relationships to the flow, differ significantly from the $\mu = 1$ case.

Similarly, in figure 12(b) the results for $\mu = 0.01$ are shown. At small μ values, one expects the effects of rotation to be negligible compared with the stretching and relaxation. As can be seen, the transition happens almost at a similar value of the case $\mu = 1$ and the p.d.f. has a characteristic -1 slope in this case.

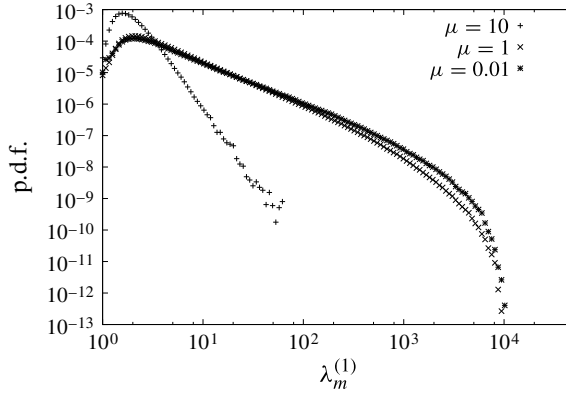


FIGURE 13. P.d.f. of the largest eigenvalue of the morphology tensor for $Ca = 0.32$ of the three viscous ratios, $\mu = 0.01, 1, 10$.

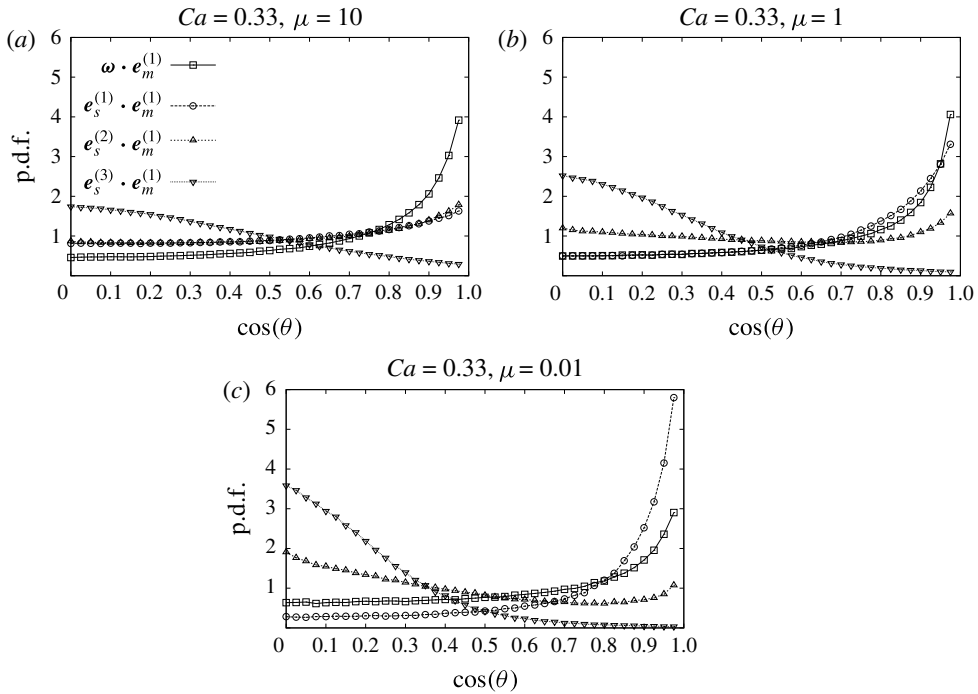


FIGURE 14. P.d.f.s of cosine of angles. Comparison between alignment with vorticity and strain-rate eigendirections for three different viscosity ratios, at $Ca = 0.33$.

In order to better highlight the dependency upon μ , in figure 13 the results are superposed for a fixed Ca value for three viscosity ratios $\mu = 0.01, 1, 10$. As one can see, the case at $\mu = 0.01$ stretches slightly better than $\mu = 1$ (f_2 is larger for $\mu = 0.01$). On the other hand, as we knew already, the $\mu = 10$ is very contracted, rotation dominates here. In figure 14 the alignment between the maximum elongation and the vorticity and the strongest stretching rate is shown for different viscous ratios at $Ca = 0.33$. Note that only for $\mu = 1$ we have a very similar weight of rotation and

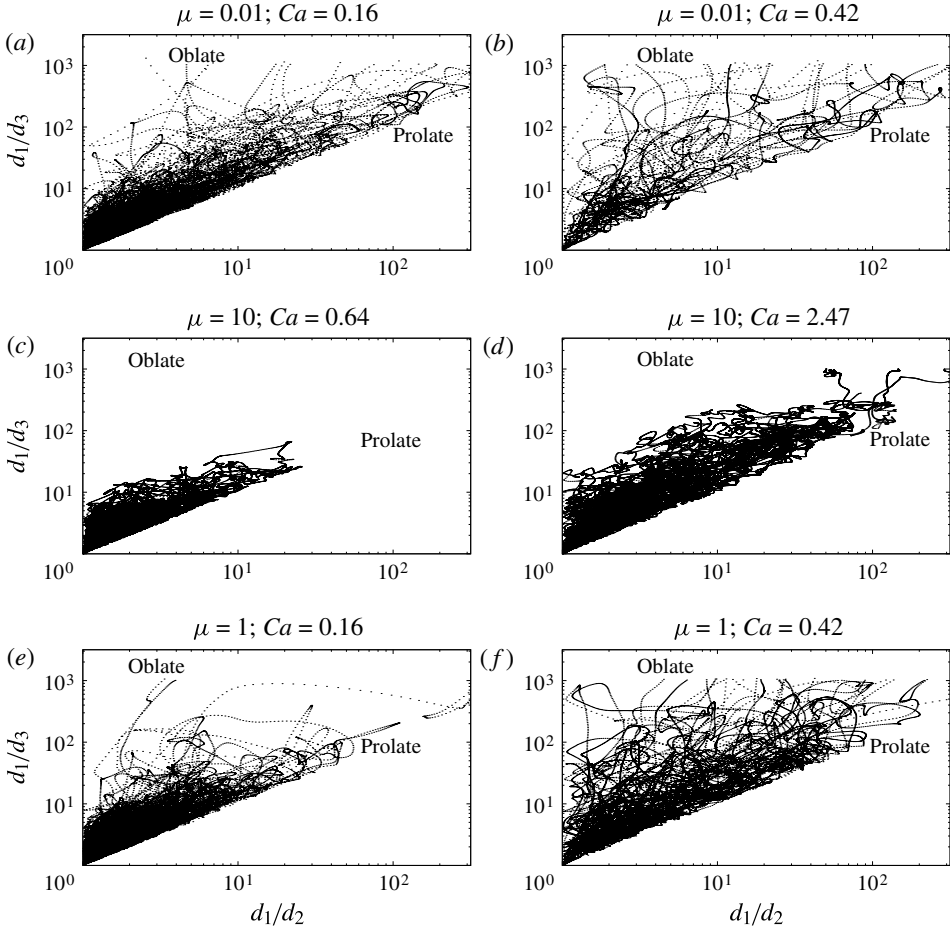


FIGURE 15. Scatter plot of the ratio between ellipsoidal semi-axes sizes.

stretching. For $\mu = 10$ stretching is fully uncorrelated with the highest deformation, as expected. On the other hand for $\mu = 0.01$ the elongation is more oriented with the strain rate. In figure 15 we show scatter plots of d_1/d_2 versus d_2/d_3 at changing τ and the viscous ratio μ . Note how the region corresponding to disks $d_1/d_2 \sim O(1)$ and $d_1/d_3 \gg 1$ is strongly depleted for the case when $\mu = 10$, i.e. when the stretching rate is not efficient. Evidently, in this case the droplets tend to be aligned with vorticity and become rod-like.

7. Conclusions

The statistical distribution of semi-axes scales and orientations of small ellipsoidal droplets (with a size smaller than the Kolmogorov scale) in fully developed homogeneous and isotropic turbulent flows has been studied. Droplets are supposed to be fully passive and diluted (no droplet–droplet interactions). In the limit of very small size, droplets can be considered inertialess with their centre of mass following the trajectories of a fluid tracer. Deformation induced by turbulent strain rate and rotation is studied by means of a simplified model proposed by Maffettone

& Minale (1998) that considers droplets to remain of ellipsoidal shape and including a restoration force due to surface tension effects that conserves droplet volume. A critical capillary number is identified at which one obtains unbounded droplet growth along one or two directions (which eventually should lead to droplet breakup). At unity droplet-to-fluid viscous ratio, one can exploit analogies with polymers to obtain analytical predictions of the critical capillary number as a function of the largest Lyapunov exponent of the trajectories of fluid particles and the relaxation timescale. Large deviation theory for the largest FTLE allows us to predict also the power-law tail of the p.d.f. of the largest droplet dimension. Another interesting question is connected with the temporal properties of the droplets dynamics. In order to determine a break-up frequency one needs to study numerically the probability of survival of different droplets and compare it with some estimate connected to the exit time along the droplet trajectory (Babler, Biferale & Lanotte 2012), i.e. the average time it takes for a droplet to experience a total stress strong enough to break it. This is connected to the Lagrangian time-decorrelation, persistency and efficiency of stress along the trajectory. A study in this direction is left for future work. For cases when the viscosities of droplet and outer fluid differ, such that vorticity is able to decorrelate the droplet from the straining directions, the large deviation theory prediction fails. The results highlight the complex dynamics of droplet deformation and orientation and opens the way to estimate/model the feedback on the flow due to the presence of deformable droplets.

The case of droplets/bubbles with a large density mismatch with respect to the density of the underlying fluid can be treated with the same approach of M&M to study the deformation along point-like particles but following inertial trajectories (Bec *et al.* 2010) instead of fluid tracers as done here. For situations in which there is a slip velocity between the droplets and fluid, it is necessary to add the stress induced by the Stokes drag in order to evaluate the deformation of the droplet.

Acknowledgements

The authors are indebted to Professor M. Minale for having provided some relevant literature and useful advice. L.B. acknowledges partial funding from the European Research Council under the European Community's Seventh Framework Program, ERC Grant Agreement No 339032. C.M. is grateful to the Università di Roma 'Tor Vergata' for their hospitality and support during a 1 month visit in May 2013, and to GoMRI for partial funding of research on droplets in turbulence.

REFERENCES

- ARORA, D., BEHR, M. & PASQUALIS, M. 2006 Hemolysis estimation in a centrifugal blood pump using a tensor-based measure. *Artif. Organs* **30**, 539–547.
- BABLER, M. U., BIFERALE, L. & LANOTTE, A. S. 2012 Breakup of small aggregates driven by turbulent hydrodynamical stress. *Phys. Rev. E* **85**, 025301R.
- BALKOVSKY, E., FOUXON, A. & LEBEDEV, V. 2000 Turbulent dynamics of polymes solutions. *Phys. Rev. Lett.* **84**, 4765–4768.
- BEC, J., BIFERALE, L., BOFFETTA, G., CENCINI, M., MUSACCHIO, S. & TOSCHI, F. 2006 Lyapunov exponents of heavy particles in turbulence. *Phys. Fluids* **18**, 091702.
- BEC, J., BIFERALE, L., LANOTTE, A. S., TOSCHI, F. & SCAGLIARINI, A. 2010 Turbulent pair dispersion of inertial particles. *J. Fluid Mech.* **645**, 497–528.
- BENZI, R., BIFERALE, L., FISHER, R., LAMB, D. Q. & TOSCHI, F. 2010 Inertial range Eulerian and Lagrangian statistics from numerical simulations of isotropic turbulence. *J. Fluid Mech.* **653**, 221–244.

- BENZI, R., BIFERALE, L., PALADIN, G., VULPIANI, A. & VERGASSOLA, M. 1991 Multifractality in the statistics of the velocity gradients in turbulence. *Phys. Rev. Lett.* **67**, 2299–2302.
- BOFFETTA, G., CELANI, A. & MUSACCHIO, S. 2003 Two-dimensional turbulence of dilute polymer solutions. *Phys. Rev. Lett.* **91**, 034501.
- CAN, E. & PROSPERETTI, A. 2012 A level set method for vapour bubble dynamics. *J. Comput. Phys.* **231**, 1533–1552.
- CENCINI, M., BEC, J., BIFERALE, L., BOFFETTA, G., CELANI, A., LANOTTE, A. S., MUSACCHIO, S. & TOSCHI, F. 2006 Dynamics and statistics of heavy particles in turbulence. *J. Turbul.* **7**, 1–16.
- CHEN, S., DOOLEN, G. D., KRAICHNAN, R. H. & SHE, Z.-S. 1993 On statistical correlations between velocity increments and locally averaged dissipation in homogeneous turbulence. *Phys. Fluids A* **5**, 458–463.
- CHERTKOV, M. 2000 Polymer stretching by turbulence. *Phys. Rev. Lett.* **84**, 4761–4764.
- CHEVILLARD, L. & MENEVEAU, C. 2013 Orientation dynamics of small, triaxial-ellipsoidal particles in isotropic turbulence. *J. Fluid Mech.* **337**, 187–193.
- CRISTINI, V., AWZDZIEWICZ, J. B., LOEWENBERG, M. & COLLINS, L. R. 2003 Breakup in stochastic Stokes flows: sub-Kolmogorov drops in isotropic turbulence. *J. Fluid Mech.* **492**, 231–250.
- DAVIES, J. T. 1985 Drop sizes of emulsions related to turbulent energy dissipation rates. *AIChE J.* **40**, 839–842.
- ECKMANN, J.-P. & PROCACCIA, I. 1986 Fluctuations of dynamical scaling indices in nonlinear systems. *Phys. Rev. A* **34**, 659–661.
- FRISCH, U. 1995 *Turbulence, The Legacy of A.N. Kolmogorov*. Cambridge University Press.
- GUALA, M., LIBERZON, A., TSINOBER, A. & KINZELBACH, W. 2007 An experimental investigation on Lagrangian correlations of small-scale turbulence at low Reynolds number. *J. Fluid Mech.* **574**, 405–427.
- GUIDO, S., MINALE, M. & MAFFETTONE, P. L. 2000a Drop shape dynamics under shear flow reversal. *J. Rheol.* **44**, 1385–1399.
- GUIDO, S., MINALE, M. & MAFFETTONE, P. L. 2000b Drop shape dynamics under shear-flow reversal. *J. Rheol.* **44**, 1385–1399.
- GUIDO, S. & VILLONE, M. 1998 Three dimensional shape of a drop under simple shear flow. *J. Rheol.* **42**, 395–415.
- HINZE, O. 1955 Fundamentals of the hydrodynamic mechanism of splitting in dispersion processes. *AIChE J.* **1**, 289–295.
- KOLMOGOROV, A. N. 1949 On the disintegration of drops in turbulent flow. *Dokl. Akad. Nauk* **66**, 825–828.
- LASHERAS, J. C., EASTWOOD, C., MARTINEZ-BAZAN, C. & MONTANES, J. L. 2002 A review of statistical models for the break-up of an immiscible fluid immersed into a fully developed turbulent flow. *Intl J. Multiphase Flow* **28**, 247–278.
- LEFEBVRE, A. H. 1989 *Atomization and Sprays*, Combustion: An International Series, vol. 1040, No. 2756. CRC Press.
- LI, M. & GARRETT, C. 1998 The relationship between oil droplet size and upper ocean turbulence. *Marine Poll. Bull.* **36**, 961–970.
- LUND, T. S. & ROGERS, M. M. 1994 An improved measure of strain state probability in turbulent flows. *Phys. Fluids* **6**, 1838–1847.
- MAFFETTONE, P. L. & MINALE, M. 1998 Equation of change for ellipsoidal drops in viscous flow. *J. Non-Newtonian Fluid Mech.* **78**, 227–241.
- MENEVEAU, C. 2011 Lagrangian dynamics and models of the velocity gradient tensor in turbulent flows. *Annu. Rev. Fluid Mech.* **43**, 219–245.
- MINALE, M. 2004 Deformation of a non-Newtonian ellipsoidal drop in a non-Newtonian matrix: extension of Maffettone–Minale model. *J. Non-Newtonian Fluid Mech.* **123**, 151–160.
- MINALE, M. 2008 A phenomenological model for wall effects on the deformation of an ellipsoidal drop in viscous flow. *Rheol. Acta* **47**, 667–675.

- MINALE, M. 2010 A phenomenological model for wall effects on the deformation of an ellipsoidal drop in viscous flow. *Rheol. Acta* **49**, 789–806.
- PALADIN, G. & VULPIANI, A. 1987 Anomalous scaling laws in multifractal objects. *Phys. Rep.* **4**, 147–225.
- PARSA, S., CALZAVARINI, E., TOSCHI, F. & VOGHT, G. A. 2012 Rotation rate of rods in turbulent fluid flow. *Phys. Rev. Lett.* **109**, 134501.
- PERLEKAR, P., BIFERALE, L., SBRAGAGLIA, M., SHRIVASTAVA, S. & TOSCHI, F. 2012 Droplet size distribution in homogeneous and isotropic turbulence. *Phys. Fluids* **24**, 065101.
- POZRIKIDIS, C. 2003 Numerical simulation of the flow-induced deformation of red blood cells. *Ann. Biomed. Engng* **31**, 1194–1205.
- SHIN, M. & KOCH, D. L. 2005 Rotational and translational dispersion of fibres in isotropic turbulent flows. *J. Fluid Mech.* **540**, 143–173.
- SUNDARESAN, S. 2000 Modeling the hydrodynamics of multiphase flow reactors: current status and challenges. *AIChE J.* **46**, 1102–1105.
- TAYLOR, G. I. 1932 The viscosity of a fluid containing small drops of another fluid. *Proc. R. Soc. Lond. A* **138**, 41–48.
- TERASHIMA, H. & TRYGGVASON, G. 2009 A front-tracking/ghost-fluid method for fluid interfaces in compressible flows. *J. Comput. Phys.* **228**, 4012–4037.
- DE TULLIO, M. D., NAM, J., PASCAZIO, G., BALARAS, E. & VERZICCO, R. 2012 Computational prediction of mechanical hemolysis in aortic valved prostheses. *Eur. J. Mech. (B/Fluids)* **35**, 47–53.
- YANG, D., CHAMECKI, M. & MENEVEAU, C. 2014 Inhibition of oil plume dilution in Langmuir ocean circulation. *Geophys. Res. Lett.* **41**, 1632–1638.
- YEUNG, P. K., POPE, S. B., KURTH, E. A. & LAMORGESE, A. G. 2007 Lagrangian conditional statistics, acceleration and local relative motion in numerically simulated isotropic turbulence. *J. Fluid Mech.* **582**, 399–422.
- YU, H. & MENEVEAU, C. 2010a Lagrangian refined Kolmogorov similarity hypothesis for gradient time evolution and correlation in turbulent flows. *Phys. Rev. Lett.* **104**, 084502.
- YU, H. & MENEVEAU, C. 2010b Scaling of conditional Lagrangian time correlation functions of velocity and pressure gradient magnitudes in isotropic turbulence. *Flow Turbul. Combust.* **85**, 457–472.